ACADEMIC PRESS

Available online at www.sciencedirect.com

SCIENCE DIRECT®

Journal of Sound and Vibration 261 (2003) 193–211

JOURNAL OF SOUND AND VIBRATION

www.elsevier.com/locate/jsvi

Numerical determination of the density profile of an inhomogeneous membrane: solution of the inverse vibration problem

S. Homolya*, I.D. Svalbe, C.F. Osborne

School of Physics and Materials Engineering, Monash University, Clayton, Victoria 3800, Australia

Received 3 December 2001; accepted 15 May 2002

Abstract

Given one or more vibrational modes of a membrane, the free vibration equation can be applied to infer the mass surface density. This paper considers determining the surface density of an inhomogeneous membrane from digitized holographic projections (interferograms) of the modeshapes. Spatially discrete numerical models of the membrane surface are presented, which can be used to solve both forward and inverse vibration problems. The accuracy of the discrete models is examined for exactly solvable free vibration problems involving inhomogeneous membranes. For the solution of the inverse problem, error estimates are given for the mass surface density deduced from modeshape interferograms. The practicability of the method is investigated using simulated experimental data for membranes with composite and continuously inhomogeneous density profiles. Strategies are discussed for reducing errors in the reconstructed densities.

1. Introduction

Vibration problems involving inhomogeneous surfaces are of general interest, as most natural and man-made materials possess, to some degree, non-uniform physical attributes. Past research on membranes with inhomogeneous densities has been mainly concerned with determining the vibrational modes and frequencies from the mass surface density [1–8]. Even for structures with simple geometries, exact solutions are only available for special cases, and, generally, approximate analytical or numerical methods are required for the solution of the free vibration problem. Laura et al. [1] report numerical results for the fundamental of a rectangular membrane with a linear

*Corresponding author. Tel.: +61-3-9905- 3694; fax: +61-3-9905-3637.
E-mail address: steven.homolya@spme.monash.edu.au (S. Homolya).

0022-460X/03/$ - see front matter
PII: S0022-460X(02)01072-6

density variation in one spatial co-ordinate. Masad [2] considers the same problem, employing second order finite difference, and first order perturbation theoretical approximations, while Wang [3] provides some exact solutions. Exactly solvable free vibration problems, involving continuously inhomogeneous strings, rods and membranes, are also discussed by Horgan and Chan [4]. Annular and circular membranes, whose densities are only a function of the radial co-ordinate, have also received considerable attention in the past. Gutierrez et al. [5] compare the accuracy of several numerical methods for this case, for several types of inhomogeneities. Laura et al. [6] also provide some numerical results, and exact solutions for special cases may be found in Refs. [3,7]. The studies reported in Refs. [1–7] involve inhomogeneity in one spatial co-ordinate, in a manner that allows the casting of the two-dimensional vibration problem, through separation of variables, into a set of equivalent one-dimensional problems. Bambill et al. [6] tackle several cases of the more difficult problem of non-separable circularly symmetric inhomogeneity in a square membrane. Work on composite membranes with piecewise continuous densities is described in Refs. [2,4,6] and references therein.

In the present study, we consider the inverse problem of determining the mass surface density of a membrane with uniform surface tension, from modeshape data that one might obtain experimentally, for example, using holographic interferometry. Our general method is applicable to any surface object with known elastic properties and an unknown surface density. However, our discussion has only limited relevance to inverse vibration problems involving inhomogeneous plates, where the stiffness and the density are generally not independent, and a lack of knowledge of one usually implies the same about the other. Analytical treatments of inverse vibration problems involving inhomogeneous plates are given by Elishakoff, in Refs. [9,10]. Here, we assume that the vibrational modes are observed as light interference patterns in the observation plane of an interferometer, and describe how the mass surface density may be deduced from digitized interferograms in practice. Connection between the continuous physical medium and the spatially discrete data is provided through an interpolation scheme, which presents improved finite difference approximations of the system. The accuracy of the approximation scheme is examined by reference to exactly solvable free vibration problems involving inhomogeneous membranes. For the practical solution of the inverse problem, we analyze the combined effects of spatial and intensity discretizations of the interferogram data, on the accuracy of the reconstructed density. Results for simulated data demonstrate that a given level of discretization in intensity places an upper limit on the spatial resolution for which the method yields an acceptable accuracy. The reconstruction method is shown to be more robust when an appropriately chosen low-pass spatial filter is applied to the vibrational amplitude data. The estimated gain in accuracy due to smoothing is found to be consistent with simulation results. A preliminary version of this work appears in Ref. [11].

2. Vibration of an inhomogeneous membrane

Let the membrane, under static equilibrium conditions, occupy a bound region S in the x–y plane. Assuming that internal and radiated energy losses can be neglected (see Section 6), the transverse displacements $U(x, y, t)$, at time t, of points (x, y) on S satisfy

$$KU = \sigma \partial_t^2 U, \tag{1}$$

where $K = K(x, y)$ is a linear stiffness operator, such that KU is the transverse force per unit surface area, σ is the mass surface density, and ∂_t^2 is a shorthand for $\partial^2/\partial t^2$. All solutions U of Eq. (1) are linear combinations of harmonic oscillations $u(x, y)\,e^{-i\omega t}$, where ω and u are natural frequencies and modes of the system respectively, satisfying

$$Ku = -\omega^2 \sigma u. \tag{2}$$

Our proposed method for the indirect measurement of the unknown density of a membrane is based on the fact that Eq. (2) can be rearranged to express σ in terms of operator K, modeshape u and frequency ω:

$$\sigma = -\frac{Ku}{\omega^2 u} \quad \text{if } u \neq 0. \tag{3}$$

If K is known, the surface density can be determined from one or more vibrational modes and frequencies. The purpose of the present work is to demonstrate how this might be done in practice, for membranes with both smooth and abrupt density variations, when modeshapes u are deduced from experimental data.

3. Holographic projections of the vibrational modes

The vibration amplitude u may be observed as a fringe pattern in the observation plane of a suitable holographic interferometer [13–16]. For single-exposure stroboscopic illumination, the fringe pattern is characterized by the intensity profile

$$I(x', y') \propto 1 + \cos\left[2\pi\alpha\, u(x, y) - \phi(x, y)\right], \tag{4}$$

where $(x', y') \propto (x, y)$ are appropriately chosen Cartesian co-ordinates of points in the observation plane, and ϕ is a phase term associated with the zero displacement ($u \equiv 0$) location of the surface relative to the apparatus [13, p. 112]. Constant α is equal to the number of fringes per unit increment in displacement u, and its magnitude (of the order of the reciprocal wavelength of the light) is determined by specifics of the experimental set-up [14]. For a planar surface, proper alignment of the apparatus will ensure that ϕ is a constant, whose value may be adjusted using an optical phase-shifter placed in the path of the reference beam [15]. (In practice, the surface may not be sufficiently planar, for example due to variations in thickness, in which case interferograms of the surface at rest can be used to determine $\phi(x, y)$. This also eliminates the need for precise alignment of the apparatus. For brevity, here we assume $\phi =$ constant.) Setting $\phi = 0$, the detected intensity (4) becomes

$$I_1'(x', y') \propto I_1(x, y) = \tfrac{1}{2}(1 + \cos\varphi), \tag{5}$$

where $\varphi = 2\pi\alpha u$. Setting $\phi = \pi/2$, a second interferogram can be obtained with intensity profile given by

$$I_2'(x', y') \propto I_2(x, y) = \tfrac{1}{2}(1 + \sin\varphi). \tag{6}$$

The two interferograms determine the phase $\varphi = 2\pi\alpha u$ modulo 2π.

Let us suppose that the intensity profiles (5) and (6) are recorded using a digital photo-detector array, whose output has been calibrated to give normalized, high contrast in the recorded images.

Assuming that the detector samples the light intensity at sites of an $L \times W$ square lattice in the observation plane, our hypothetical experimental results are two $L \times W$ greyscale images G_1 and G_2 corresponding to intensities I_1 and I_2, respectively:

$$G_j(p,q) = \text{nint}[(D+\Delta)\, I_j(ph, qh) + \delta], \quad j = 1,2, \tag{7}$$

where p and q are integers in $[1, L]$ and $[1, W]$, respectively, $D+1$ is the number of greylevels in the image, h is the sampling interval at S, Δ and δ are errors in calibrating the detector output, and $\text{nint}(Z)$ denotes the integer closest to $Z \in \mathbb{R}$. In practice, two further arrays, δG_1 and δG_2, would specify experimental errors in G_1 and G_2, respectively, such that

$$G_j(p,q) - \delta G_j(p,q) \leqslant D\, I_j(ph, qh) \leqslant G_j(p,q) + \delta G_j(p,q). \tag{8}$$

Expressing the sampled phase, $\varphi(ph, qh) \bmod 2\pi \simeq \varphi_{pq} \bmod 2\pi$ of (5), (6) in terms of pixel values G_j, and considering relation (8), the errors $\delta\varphi_{pq}$ in the phase, $\varphi(ph, qh) \bmod 2\pi = \varphi_{pq} \bmod 2\pi \pm \delta\varphi_{pq}$, can be estimated by

$$\delta\varphi_{pq} = \min\left(\frac{\delta G_1}{|G_2 - D/2|}, \frac{\delta G_2}{|G_1 - D/2|}\right), \tag{9}$$

correct to first order in δG_j. For the sake of definiteness, we assume in what follows that calibration errors Δ and δ are at most half one greylevel, and that the errors introduced by level quantization are much greater than all other errors combined. Then, by allowing for rounding errors in Eq. (7), we have $\delta G_j = 0.5 G_j/D + 1$, so the errors $\delta\varphi_{pq}$ in the phase may be estimated from greyvalues G_j alone, using Eq. (9).

From the phase $\varphi \bmod 2\pi$ deduced from the two interferograms $G_{1,2}$, the true phase of the wave $\varphi = 2\pi\alpha u$ can be obtained by unwrapping the mod 2π phase. In Section 5, we employ a sequential linear scanning algorithm due to Takeda [16, p. 204–205]. As the unwrapped phase φ_{pq} is proportional to the amplitude of vibration at grid points $(x, y) = (ph, qh)$, it is also a sampled solution $u_{pq} = u(ph, qh) = \varphi_{pq}$ of Eq. (2), within known error $\delta u_{pq} = \delta\varphi_{pq}$. With ω measured as the resonance frequency for displacement amplitude u, a sampled solution (ω, u_{pq}) of Eq. (2) is obtained.

Simulated interferograms for the sixth vibrational mode of an inhomogeneous membrane are shown in Fig. 1. A wireframe plot of the vibration amplitude is shown in Fig. 1a. Figs. 1b and c are interferograms given by Eq. (7) with $D = 255$ and $L = W = 60$. Fig. 1d is a linear greyscale plot of the phase deduced from the two interferograms, with black and white corresponding to 0 and 2π, respectively. Fig. 1e shows the unwrapped phase u_{pq}, obtained after applying Takeda's algorithm to the mod 2π data. Here, black and white correspond to maximum negative and positive amplitudes, respectively. Within estimated errors given by Eq. (9), this unwrapped phase is proportional to the displacement amplitude shown in Fig. 1a.

4. Spatial discretization of the surface

Eqs. (2) and (3) describe relations between functions of continuous variables, $u(x, y)$ and $\sigma(x, y)$ that are defined for all $(x, y) \in S$. An approximation to Eqs. (2) and (3), in terms of sampled data u_{pq}, may be obtained by interpolation. Here we describe one method, using polynomial

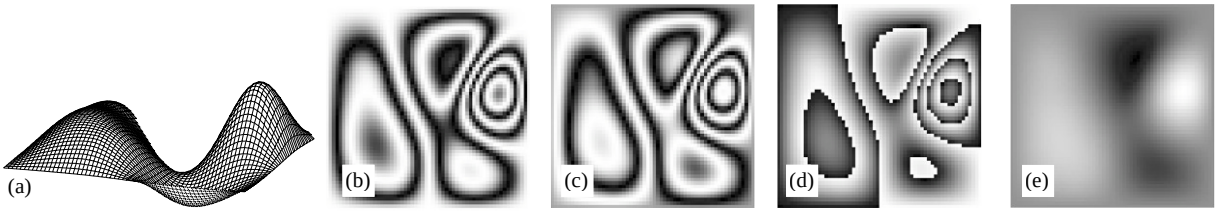

Fig. 1. Simulated interferogram data for the sixth vibrational mode of an inhomogeneous membrane: (a) displacement amplitude, (b) cosine fringes, (c) sine fringes, (d) wrapped phase, (e) unwrapped phase, proportional to surface displacement.

interpolation, for a membrane with a surface tension of unity, i.e.,

$$K = \nabla^2 = \partial_x^2 + \partial_y^2.$$

We first approximate $u(x, qh)$ in the neighbourhood of $x = x_0 = ph$, by a polynomial of degree $2N$:

$$u(x, qh) \simeq f(x) = \sum_{n=0}^{2N} a_n (x - x_0)^n. \tag{10}$$

Coefficients a_n are obtained by requiring that the interpolating polynomial $f(x)$ fit the sampled data at $2N + 1$ points centred on $x = x_0$:

$$f(x_0 + nh) = u_{p+n,q} \quad \text{for } n = -N, \ldots, N. \tag{11}$$

The second derivative of f is given by

$$f''(x)|_{x=x_0} = \frac{1}{h^2} \sum_{n=-N}^{N} C_n u_{p+n,q}, \tag{12}$$

where coefficients C_n only depend on the degree $2N$ of the interpolating polynomial. Due to invariance of the form of Eq. (11) with respect to transformation $n \to -n$, we must have $C_n = C_{-n}$. The values of coefficients C_n for $N = 1, 2, 3, 4$ are presented in Table 1.

Similarly, second order partial derivatives with respect to y can be expressed as linear combinations of sampled values $u_{p,q+n}$, so the transverse force per unit surface area may be approximated as

$$K\, u(x, y)|_{(x,y)=(ph,qh)} \simeq \sum_{rs} K_{pq,rs}\, u_{rs}, \tag{13}$$

where

$$K_{pq,rs} = \begin{cases} C_{p-r}/h^2 & \text{if } q = s \text{ and } 1 \leqslant |p - r| \leqslant N, \\ C_{q-s}/h^2 & \text{if } p = r \text{ and } 1 \leqslant |q - s| \leqslant N, \\ 2C_0/h^2 & \text{if } p = r \text{ and } q = s, \\ 0 & \text{otherwise.} \end{cases} \tag{14}$$

Table 1
Coefficients used to estimate second order derivatives of a sampled function

N	C_0	C_1	C_2	C_3	C_4
1	−2	1			
2	−5/2	4/3	−1/12		
3	−49/18	3/2	−3/20	1/90	
4	−205/72	8/5	−1/5	8/315	−1/560

This leads us to our key result, which is an approximation to (2) at grid points $(x, y) = (ph, qh)$:

$$\sum_{rs} K_{pq,rs} u_{rs} = -\omega^2 \sigma_{pq} u_{pq}, \tag{15}$$

where $\sigma_{pq} = \sigma(ph, qh)$. The matrix of coefficients $\mathbf{K} = [K_{pq,rs}]$, the stiffness matrix, is the discrete counterpart of the stiffness operator K. From Eq. (15), we obtain the sampled density as

$$\sigma_{pq} = \frac{-\sum_{rs} K_{pq,rs} u_{rs}}{\omega^2 u_{pq}}, \quad u_{pq} \neq 0, \tag{16}$$

which is the discrete version of Eq. (3). Eq. (16) yields σ_{pq} wherever the right-hand side of the equation is defined, i.e., at all sampling locations $(x, y) = (ph, qh)$ that have at least N nearest neighbours, in both x and y directions, on the interior of the membrane. Since we need not consider boundary conditions in the solution of the inverse problem, relation (16) may be applied irrespective of the shape of the membrane.

4.1. Discretization errors

For $N = 1$, the approximation of the Laplacian given by Eqs. (13) and (14) is the ordinary finite difference approximation. For $N = 2$ it corresponds to the improved fourth order scheme developed in Ref. [12]. For a sufficiently differentiable function u it may be shown, by direct substitution of a power-series expansion of u in Eq. (13), that the error in the expression is of order $2N$ in the grid spacing h. We examine the accuracy of this discrete representation of the continuous system by considering two exactly solvable free vibration problems: a membrane with continuously inhomogeneous density, and a composite membrane with step discontinuity.

4.1.1. Continuous inhomogeneity

We consider a square membrane with a surface density that is linear in x, with $\sigma(x, y) = 2x$. The area and surface tension of the membrane are unity. The free vibration equation (2) becomes

$$\nabla^2 u(x, y) = -2\omega^2 x\, u(x, y), \tag{17}$$

where $0 < x < 1$ and $0 < y < 1$. The membrane is fixed to a rigid support at its boundary with

$$u(0, y) = u(1, y) = u(x, 0) = u(x, 1) = 0.$$

This system is a limiting case of one considered by Wang [3], with the unphysical property of vanishing density, and diverging phase velocity, at the $x = 0$ boundary. Exact solutions for the

modes are of the form

$$u(x,y) = \sin(n\pi y)\,[C_1\,\mathrm{Ai}(ax+b) + C_2\,\mathrm{Bi}(ax+b)],$$

where Ai and Bi denote Airy functions of the first and second kind, respectively, n is a positive integer, C_1 and C_2 are constants, and

$$a = -(2\omega^2)^{1/3}, \quad b = (n\pi/a)^2.$$

Solutions of the transcendental equations

$$C_1\,\mathrm{Ai}(b) + C_2\,\mathrm{Bi}(b) = C_1\,\mathrm{Ai}(a+b) + C_2\,\mathrm{Bi}(a+b) = 0, \tag{18}$$

which ensure boundary conditions are satisfied at $x = 0, 1$, yield constants C_1, C_2 (within an arbitrary multiplicative factor) and frequencies ω.

Solution of Eq. (18) by conventional root search methods can easily miss valid roots. This is exemplified in Ref. [3], where results are presented for the fundamental frequency of rectangular membranes with densities linear in x. The results indicate several step-like increases in the value of the fundamental frequency, as the inhomogeneity parameter is gradually increased. Our calculations show that all frequencies reported in Ref. [3] are valid frequencies of the membranes, but many of them are not the fundamental, and the anomalies observed are a numerical artifact due to missed roots. To solve Eq. (18), we employ the so-called "shooting method", which is often used to obtain eigenfunctions of quantum mechanical systems [17]. It relies on the fact that if the modal displacement $u(x,y)$ is separable into a product of an x-dependent part $X(x)$ and a y-dependent part $Y(y)$, so that $u = XY$, then all modes are uniquely identifiable by a 2-D index $(M_x, M_y) \in \mathbb{N} \times \mathbb{N}$, such that $M_x - 1$ and $M_y - 1$ are equal to the number of zeros of X and Y on the membrane. For the present case, $X = C_1\,\mathrm{Ai}(ax+b) + C_2\,\mathrm{Bi}(ax+b)$ and $Y = \sin(n\pi y)$. For given $M_y = n$, the number of valid frequencies less than some trial frequency ω_{trial} is found as the number of zeros of $X(x)$ for $x \in [0,1)$, after letting $\omega = \omega_{trial}$ in X and choosing constants C_1 and C_2 so that the boundary condition at $x = 0$ is satisfied with $X(0) = 0$. Once intervals containing valid solutions are identified, the sizes of the intervals are iteratively reduced until machine-precision solutions are obtained. No valid roots are missed because each mode is uniquely identified by the 2-D mode index (M_x, M_y), and the frequency is a monotonously increasing function of M_x and M_y.

For an approximate numerical solution of the problem, the displacement amplitude u and the density σ are sampled at $(L+1) \times (L+1)$ points on the surface and boundary. Eq. (17) is approximated by Eq. (15) with $\sigma_{pq} = 2ph$, where $h = 1/L$. The discrete system has $(L-1)^2$ degrees of freedom, equal to the number of internal grid points. For $N > 1$, the degree of the interpolating polynomials is retained at all grid points, by defining the wave amplitude at grid points outside the membrane, in a manner consistent with boundary conditions. For example, we set $u_{0q} = 0$ and $u_{-p,q} = -u_{pq}$, which approximates the displacement amplitude with an odd function $f(x)$ at $y = qh$. Odd- and even-order derivatives of $f(x)$ are even and odd functions, respectively. This implies that the existence of an even-order derivative $f^{(2n)}(x)$, at $x = 0$, ensures the continuity of the odd-order derivative $f^{(2n+1)}(x)$ at $x = 0$. The equation of motion and the fixed boundary conditions ensure that f will have a vanishing second derivative on the boundary at $x = 0$, since there $\nabla^2 u = u = 0$. Hence f has continuous derivatives of up to third order, and

the fourth derivative is, in general, discontinuous at $x = 0$. This limits the accuracy of the discrete approximation to $O(h^4)$, for any interpolation order $2N > 4$.

For efficient solution of the generalized eigenproblem (15), it is first transformed into the simple eigenvalue problem

$$\sum_{rs} M_{pq,rs} w_{rs} = \omega^2 w_{pq}, \tag{19}$$

where

$$w_{pq} = u_{pq}\sqrt{\sigma_{pq}},$$

$$M_{pq,rs} = -\frac{1}{\sqrt{\sigma_{pq}}} K_{pq,rs} \frac{1}{\sqrt{\sigma_{rs}}}.$$

Matrix $[M_{pq,rs}]$ has the symmetry properties of $[K_{pq,rs}]$, i.e., it is real symmetric. Eq. (19) was solved for eigenvalues ω^2 and eigenvectors $\{w_{pq}\}$ using the Lanczos algorithm. The Lanczos algorithm provides an efficient way to solve large sparse matrix eigenproblems. Eq. (19) presents a sparse problem, since, by Eq. (14), most of the stiffness matrix coefficients are zero. Our implementation of the algorithm is based on that of Cullum and Willoughby [18]. Eigenvalues are obtained at typically 10 (at worst 8) digits of precision, and eigenvector components are accurate to 6 (5) digits.

Results for the fundamental frequency of the $\sigma(x, y) = 2x$ membrane are presented in Table 2 for $L = 10, 20, 50, 100$ and $N = 1, 2, 4$. We have also included frequencies computed using the finite element method (F-E), with linear element functions. The finite element method is considerably more taxing on computational resources, so we have only computed frequencies for $L = 10, 20, 50$. The exact frequency is shown below each data set. The results show that the accuracy of the finite difference approximation improves with increasing L and N. The accuracy of the finite element method is similar to that obtained using ordinary finite differences ($N = 1$), with the latter method underestimating the frequency by about the same amount, for the same L, as the former overestimates it. For the smallest grid size of $L = 10$, the frequencies obtained with these methods are within about 0.5% of the exact value. For the improved finite difference schemes of order 4 and 8 the accuracies are 0.01% and 0.003%, respectively.

For all values of L considered here, the increase in the accuracy is remarkable when going from $N = 1$ to 2. However increasing N beyond 2 results in only modest improvements. This reflects the fourth-order, $O(h^4)$, limit on accuracy, due to boundary conditions. The discrete approximation to the Laplacian can only be improved at grid points where the interpolating functions do not involve "image" points beyond the boundary of the system.

The errors in the computed frequencies are

$$\Delta\omega = |\omega^{(\mathrm{xct})} - \omega^{(\mathrm{apx})}|,$$

where superscripts "(xct)" and "(apx)" denote exact and numerical, approximate, values respectively. We define the errors in the modal displacement u as

$$\Delta u_{\max} = \max_{p,q=1}^{L-1} |\Delta u(ph, qh)|, \tag{20}$$

Table 2
Numerical results for the fundamental frequency of the $\sigma(x,y) = 2x$ membrane

L	$N = 1$	$N = 2$	$N = 4$	F-E
10	4.256 299 776	4.278 110 479	4.278 655 202	4.300 790 193
20	4.272 986 059	4.278 510 940	4.278 545 886	4.284 109 706
50	4.277 646 999	4.278 538 013	4.278 538 914	4.279 430 469
100	4.278 315 786	4.278 538 683	4.278 538 738	
Exact	4.278 538 732	4.278 538 732	4.278 538 732	4.278 538 732

with

$$\Delta u(ph, qh) = u_{pq}^{(\mathrm{xct})} - u_{pq}^{(\mathrm{apx})},$$

where arrays $\{u_{pq}^{(\mathrm{xct})}\}$ and $\{u_{pq}^{(\mathrm{apx})}\}$ are scaled so that the magnitude of the largest elements is equal to unity, i.e. $\max_{pq} |u_{pq}^{(\mathrm{xct})}| = \max_{pq} |u_{pq}^{(\mathrm{apx})}| = 1$, and the two arrays are in phase ($u_{pq}^{(\mathrm{xct})} \simeq u_{pq}^{(\mathrm{apx})}$ rather than $u_{pq}^{(\mathrm{xct})} \simeq -u_{pq}^{(\mathrm{apx})}$).

The relative errors $\Delta\omega/\omega$ in the computed frequencies are presented in Fig. 2. The errors for the first 20 modes of the membrane are plotted as a function of the mode index M in Fig. 2a, for a grid size of $L = 60$. (The mode index numbers the modes in order of ascending frequency, with $M = 1$ for the fundamental.) Results are shown for finite difference schemes of order $2N = 2, 4, 8$ and for the finite element method. All frequencies are obtained with relative errors less than 10^{-4} for $N = 2$, and 10^{-6} for $N = 4$. Errors for the finite element and ordinary finite difference methods are less than 1%.

In Fig. 2b, we have plotted the relative error in the 10th gravest frequency of the membrane against grid size L. For the second and fourth order schemes ($N = 1, 2$), the results clearly indicate that errors are of the respective order in the sampling interval $h = 1/L$. For $N = 4$ and $L \geq 30$, the order of the approximation is dominated by fourth order errors associated with the fixed boundary.

Exact and approximate results for the first 20 modes of the membrane indicate that the errors in the modeshapes, as defined by Eq. (20), are no more than an order of magnitude greater than the relative errors in the corresponding frequencies, or 10^{-5} (whichever is greater), i.e.,

$$\Delta u_{\max} < \begin{cases} 10\,\Delta\omega/\omega, & \Delta\omega/\omega > 10^{-6}, \\ 10^{-5} & \text{otherwise.} \end{cases}$$

The upper limit of 10^{-5} on accuracy reflects the five digits of precision attainable by the eigensolver.

4.1.2. Step inhomogeneity

To illustrate some of the limitations of the discrete models, we consider a square membrane with step discontinuity. The membrane surface occupies the domain $0 < x < 1$, $0 < y < 1$, and the

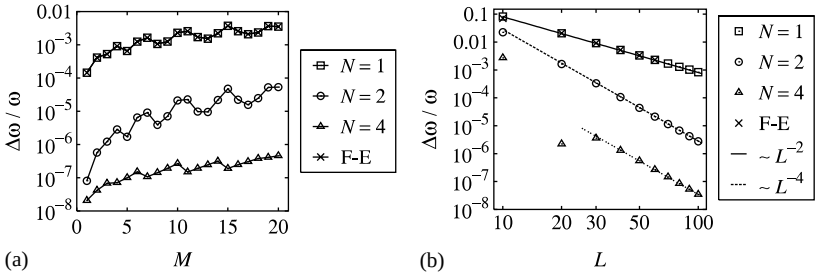

Fig. 2. Relative errors $\Delta\omega/\omega$ in frequencies ω of a square membrane with density $\sigma(x, y) = 2x$, computed using order-$2N$ finite difference and finite element (F-E) methods. (a) Log-linear plot of error against mode index M for grid size $L = 60$. (b) Log–log plot of the error in the 10th gravest frequency against L. Straight lines drawn through data points represent second and fourth order trends as indicated.

surface density is

$$\sigma = \begin{cases} 1.9, & x > 0.5, \\ 1, & x = 0.5, \\ 0.1, & x < 0.5. \end{cases}$$

The total mass of the membrane is unity. Exact solutions for the natural frequencies and modes may be found by imposing boundary conditions at $x = 0, 1$ and continuity conditions at $x = 0.5$ on the general solution for the x-dependent part of the displacement amplitude.

Fig. 3 shows our results for the modeshape of the fundamental. The x-dependent part of the mode is shown in Fig. 3a. The amplitude in the low-density region, $x < 0.5$, is characterized by exponential decay, and in $x > 0.5$, where the density is high, it is sinusoidal. The solid curve corresponds to the exact result, and the data points represent the fundamental of discrete systems with $L = 60$. In Fig. 3b, we have plotted the difference between the exact and approximate modeshapes for $N = 1, 2$. For both schemes, the difference is greatest at grid points near the discontinuity in σ.

The relative errors for the fundamental frequency are plotted as a function of L in Fig. 4a for $N = 1$ and 2. The error for both schemes decreases as L^{-2}. This is due to a discontinuity in the density σ, which implies discontinuity in the second derivative of the amplitude u. Consequently, the fourth order scheme is reduced in accuracy to second order. For $N = 1$, results obtained with L even (where the continuous system is being sampled on the discontinuity at $x = 0.5$), are about five times more accurate than those for odd L. For $N = 2$, odd values of L yield better accuracy. The most accurate solutions are obtained with $N = 1$ and L even. The sensitivity of the system to small (± 1) changes in L is less, however, for $N = 2$. Results obtained with $N > 2$ are similar to those obtained with $N = 2$, i.e., increasing the interpolation order beyond four had no significant effect on the accuracy. The errors in the first 20 natural frequencies, computed with $N = 1, 2$ and $L = 60$, are shown in Fig. 4b. For $N = 2$ all frequencies are accurate to at least 0.06%. The accuracy of the ordinary finite difference scheme ($N = 1$), with the exception of the fundamental, is significantly less, with errors of up to 0.5%.

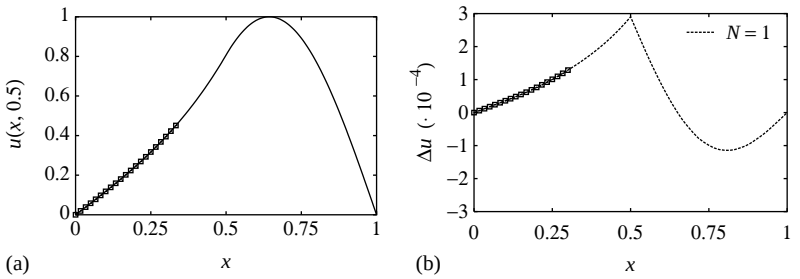

Fig. 3. Results for the x-dependent part of the fundamental of the composite membrane described in the text. (a) Discrete approximation to the modeshape $u(x, 0.5)$ using 59 internal sample points ($L = 60$). The solid curve represents the exact result. (b) Difference between the exact result $u^{(\mathrm{xct})}$ and discrete approximation $u^{(\mathrm{apx})}$ for $N = 1, 2$, with $L = 60$.

4.2. Error estimates for reconstructed densities

Let us suppose that a sampled modeshape u_{pq} and the corresponding natural frequency ω have been deduced experimentally within known errors, $\pm\delta u_{pq}$ and $\pm\delta\omega$, respectively. Results presented in Section 4.1 indicate that, in what follows, the simulated experimental errors dominate over spatial discretization errors. Therefore, the errors $\delta\sigma_{pq}$ in σ by Eq. (16) may be estimated as

$$\delta\sigma_{pq} = \left(\frac{\sum_{rs} |K_{pq,rs}| \delta u_{rs}}{|\sum_{rs} K_{pq,rs} u_{rs}|} + \frac{\delta u_{pq}}{|u_{pq}|} + 2\frac{\delta\omega}{\omega} \right) \sigma_{pq}, \tag{21}$$

which is correct to first order in δu_{pq} and $\delta\omega$. When several modes and their vibrational frequencies are known, Eq. (16) provides several corresponding estimates for the surface density. Results from several modes may be combined by selecting the best estimate for σ_{pq}, for each (p, q).

5. Results with simulated data

Surface reconstructions are presented for simulated experimental data. We considered two membranes with inhomogeneous surface densities and surface tensions of unity. The membranes were assumed fixed to a rigid square boundary. The first step in simulating the experimental data involved solution of the free vibration equation (2) for the first 20 natural frequencies and modes, by discretization on a high-resolution, 240×240, grid, as described in Section 4. Eighth order interpolations were used to approximate the Laplacian. This high-resolution modeshape data was down-sampled onto a 60×60 grid. Intensities $I_{1,2}(x, y)$ were computed from the down-sampled modeshape data using Eqs. (5), (6), with the amplitude of vibration scaled to give similar fringe densities for all modes.

Using relation (7), the two greyscale images $G_{1,2}$ were generated from the computed intensities $I_{1,2}$, with calibration errors Δ and δ chosen at random from the interval $[-0.5, 0.5]$ for each set of modes. D was set to one of the three values: 15, 63 or 255, which correspond to detector depth resolutions of 16, 64 and 256 levels, respectively. Approximations u_{pq} to the sampled modes, along with error estimates δu_{pq}, were obtained from the simulated experimental data, as described in

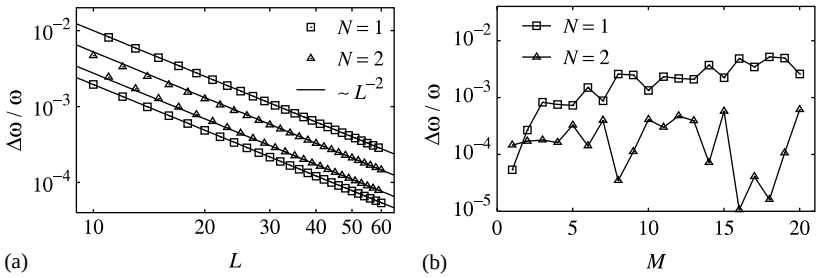

Fig. 4. Relative errors $\Delta\omega/\omega$ in order-$2N$ finite difference approximations to frequencies ω of the composite membrane described in the text. (a) Log–log plot of the error in the fundamental against grid size L, for $N = 1, 2$. Solid lines represent second order trends. (b) Log-linear plot of error against mode index M, for $N = 1, 2$, and $L = 60$.

Section 3. The vibrational frequencies ω were assumed exact with $\delta\omega = 0$. The surface reconstruction method described in Section 4 was applied to the sampled modeshape data, to recover the sampled surface density using Eq. (16), with estimated errors given by Eq. (21). Fourth order interpolations were used in the solution of the inverse problem.

5.1. Test densities

The two density functions used in the simulations are shown as greyscale plots in Fig. 5a and b. The density of system 1, plotted in Fig. 5a, comprises four homogeneous regions, where $\sigma = 1,\ 2$ or 3 (lighter shades of grey represent larger values). The density changes abruptly at the boundaries between homogeneous regions. The image shown in Fig. 5b represents the density of system 2, which is a superposition of plane waves with randomly generated relative phases (bandwidth-limited white noise), with global extrema of 0.25 and 2.0. Figs. 5c and d show the two density functions with reduced resolution (60×60). These are the sought-after solutions of the inverse problem.

5.2. Reconstruction from raw data

Figs. 6 and 7 provide a summary of results for reconstructed densities, in tabulated form, with simulated detector depth of 256 levels. The top rows of images are sine-fringe interferograms G_2 of modes $M = 1, 2, 5, 10, 20$. Densities σ_M, shown in the second row, are computed from the interferograms of mode M. Regions in black represent grid points where the estimated relative errors in the computed density are greater than 50%. For both systems, the density computations show poor accuracy near nodal lines, as expected from Eq. (21). Images on the bottom rows of Figs. 6 and 7 correspond to the reconstructed densities $\sigma_{1,\ldots,M}$ obtained by combining σ_M deduced from modes 1 through M. The first 10 modes recover most of the sampled density array for both systems, and with 20 modes, we have good estimates over more than about 90% of the area of the membrane.

Both reconstructions show considerable speckle noise. However, these variations are within estimated errors, which have proved to be conservative, typically less than 20% of the true error, except at internal boundaries between constant density regions of system 1. Here, the slight

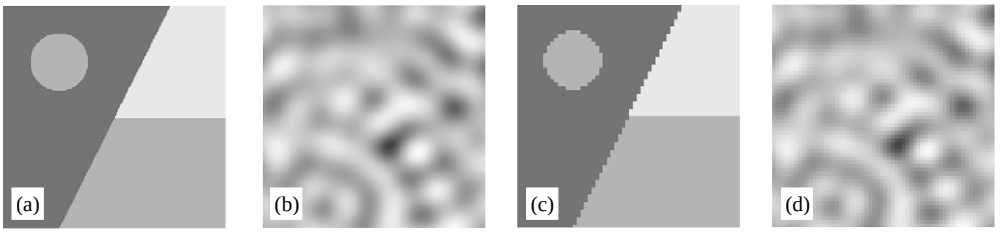

Fig. 5. Greyscale plots of membrane surface density functions σ used in the simulations: (a) composite of four homogeneous regions, where $\sigma = 1$ (darkest), 2 (medium grey), 3 (lightest); (b) low-pass filtered white noise; (c,d) the same functions sampled on a 60×60 grid—the arrays sought from the simulated experimental data.

"blurring", observed in the reconstructions shown in Fig. 6, arises from errors introduced by discretization of the stiffness operator, and is present for all D. This was confirmed by simulations with $D \leqslant 10^7$.

Poor reconstruction results were obtained with 64- and 16-greylevel interferograms ($D = 63, 15$). For $D = 15$, all estimated errors for reconstructed densities were greater than 50%, and for $D = 63$, only about 10% of the membrane surface was recovered from the first 20 modes.

5.3. *Reconstruction from down-sampled data*

The large error estimates in the density computed from low-depth interferograms are due to the inaccuracy of the approximation on the left-hand side of Eq. (15), involving the stiffness matrix $[K_{pq,rs}]$, to $\nabla^2 u$. As the approximation scheme is based on local interpolation, it is differences between nearest-neighbour sampled values of u that determine the approximated value of $\nabla^2 u$. Whenever differences between such values are similar in magnitude to the errors, the approximation fails. As the spatial sampling interval h is decreased, and the surface is probed in more detail, the second derivative (21) of the interpolating function approaches the corresponding second derivative of the displacement amplitude, only if the sampled data are exact. Then the sum on the right-hand side of Eq. (12) must vanish as h^2. When estimated errors in sampled values $u_{p+n,q}$ are independent of h, the estimated absolute error for the sum remains similar in magnitude for all h, so the estimated relative error in the expression diverges as h^{-2}. Therefore, increasing the spatial resolution results in larger errors.

We can compensate for this by increasing the accuracy of the data, increasing the depth resolution of the interferogram images with $D \sim h^{-2}$. Alternatively, the spatial resolution may be reduced for low depth resolution data, with $h \sim 1/\sqrt{D}$. For the simulated interferogram data with $D = 64$ and $D = 15$, estimated accuracies, similar to those obtained with $D = 255$, may be achieved, if the spatial resolution is reduced from 60×60, to 30×30 and 15×15, respectively. To ensure the reliability of the phase unwrapping algorithm, the resolution reduction is introduced in the unwrapped phase, rather than the interferograms, where it could result in missed fringes.

Results for densities computed from reduced resolution phase arrays are shown tabulated in Fig. 8. The first and second columns of images show the 15×15 density arrays for systems 1 and 2, respectively, computed from 16-greylevel interferograms. The 30×30 density arrays obtained

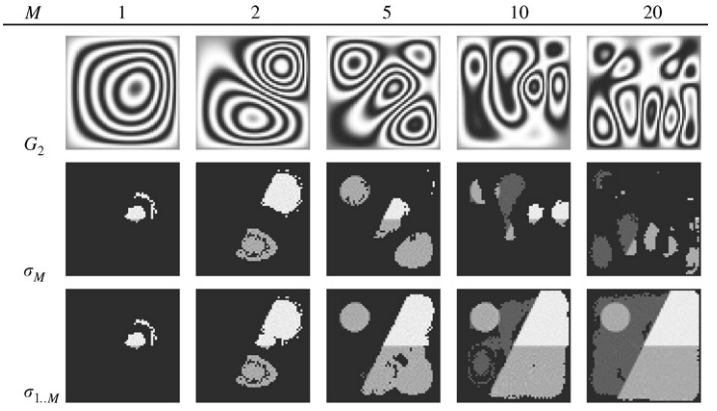

Fig. 6. Simulated 256-greylevel modeshape interferograms and reconstructed surface densities for system 1. Definition of symbols: M, mode index; σ_M, density computed from interferograms of mode M only; G_2, sine-fringe interferograms given by Eq. (7) with $j = 2$; $\sigma_{1,\ldots,M}$, density computed from interferograms of modes 1 to M.

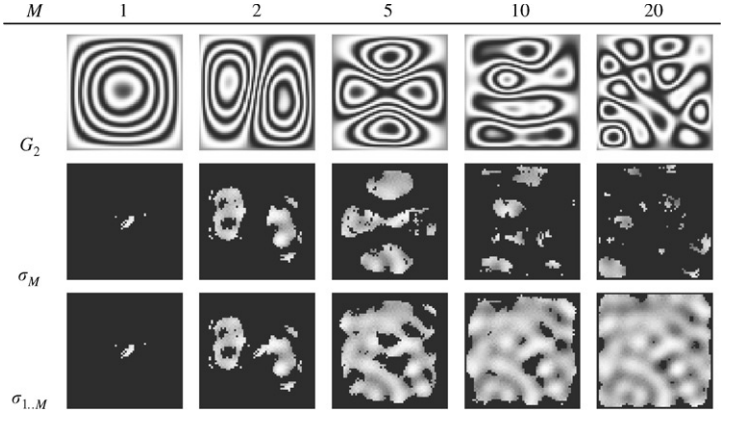

Fig. 7. Simulated 256-greylevel modeshape interferograms and reconstructed surface densities for system 2. Definition of symbols as per Fig. 6.

from 64-greylevel interferograms are shown in the third and fourth columns. The first row of images shows densities reconstructed from interferograms of mode 5 alone, the second the combined result from modes 1 to 5, and the third from modes 1 to 20. Apart from the reduced spatial resolution, the reconstructions are comparable to corresponding results shown in Figs. 6 and 7, for $D = 255$.

5.4. *Reconstruction from filtered data*

The main disadvantage of down-sampling is that errors associated with the discretization of the stiffness operator may become excessive at low spatial resolutions. An alternative is to apply a

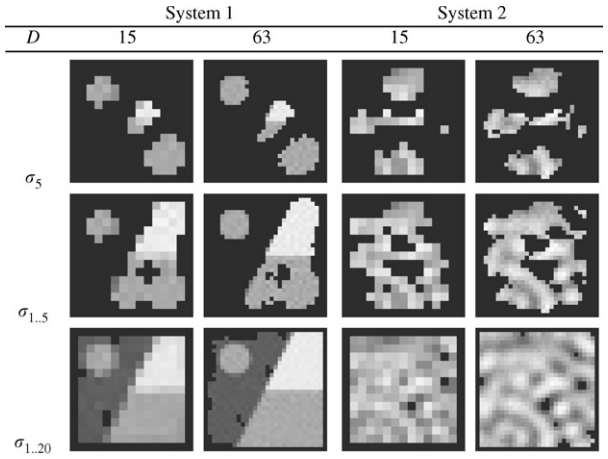

Fig. 8. Reduced resolution surface reconstructions from simulated interferogram data quantized to $D+1=16$ and 64 levels. Symbols σ_5, $\sigma_{1,\ldots,5}$ and $\sigma_{1,\ldots,20}$ signify reconstructions from interferograms of mode 5, modes 1 to 5, and modes 1 to 20, respectively.

low-pass filter to the sampled wave amplitude data. We apply a filter "window", so that

$$u_{pq} \to \frac{\sum_{ij} F_{i-p,j-q} u_{ij}}{\sum_{ij} F_{ij}}, \tag{22}$$

where the sums are over the entire array ($i=1,\ldots,L,\ j=1,\ldots,W$). A Gaussian blur window is defined by coefficients F_{pq} given by

$$F_{pq} = \mathrm{e}^{-(p^2+q^2)/R^2},$$

where R is the radius of the filter. Using the filtered phase to calculate the density from Eq. (3), we get

$$\sigma_{pq} = \frac{-\sum_{ij,rs} K_{pq,rs} F_{i-r,j-s} u_{ij}}{\omega^2 \sum_{ij} F_{i-p,j-p} u_{ij}},$$

where u_{ij} signify the raw, unfiltered, data. Relative errors for the densities σ_{pq} computed from the filtered phase may now be estimated, to first order in errors δu_{ij} and $\delta\omega$, as

$$\frac{\delta\sigma_{pq}}{\sigma_{pq}} = \frac{\sum_{ij} \left|\sum_{rs} K_{pq,rs} F_{i-r,j-s}\right| \delta u_{ij}}{|\sum_{ij,rs} K_{pq,rs} F_{i-r,j-s} u_{ij}|} + \frac{\sum_{ij} \left|F_{i-r,j-s}\right| \delta u_{ij}}{|\sum_{ij} F_{i-r,j-s} u_{ij}|} + 2\frac{\delta\omega}{\omega}. \tag{23}$$

Filtering works because in the first term on the right-hand side of Eq. (23), which is the relative error in Ku, it is the coefficients $K_{pq,rs}$ that are being blurred and not the errors. As $K_{pq,rs}$ alternate in sign with increments in r or s, and the filter gives a weighted average over these, the magnitude of this average is going to be smaller than a sum of the magnitudes of $K_{pq,rs}$, given in Eq. (21). The error estimates given by Eq. (23) are generally reduced by filtering. The purpose of filtering is to make the true errors at neighbouring grid-points similar in value, without excessively blurring the data. We can check whether we have chosen a reasonable value for the filter radius by comparing

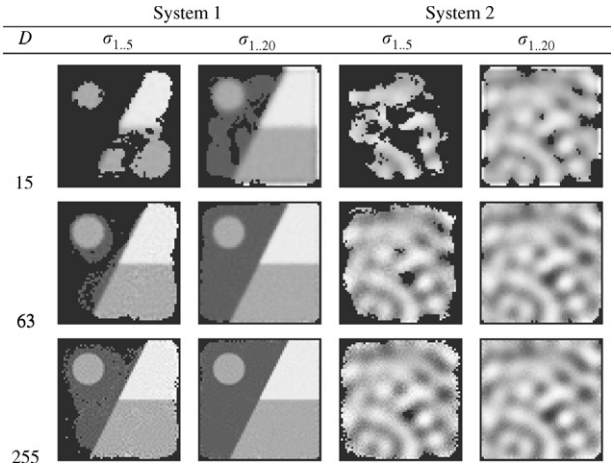

Fig. 9. 60×60 surface density arrays reconstructed from simulated modeshape interferogram data, with low-pass filtering used to suppress level quantization errors. Reconstructions with $D = 15$, 63 and 255 were obtained using filters of radii $R = 2$, 1 and 0.5, respectively.

filtered and unfiltered data. If the former is not within estimated error of the latter, the filter radius needs to be decreased.

While expression (23) can be used to compute the reduced error estimates for σ_{pq}, the computation of the first sum on the right-hand side of Eq. (23) for each (p, q) is time consuming, because the coefficient blurring generates many terms in the sum. Instead of computing the errors directly, we can estimate the ratio ρ of errors in Ku obtained with and without filtering, by comparing the magnitude of coefficients of δu_{ij} in the corresponding terms of Eqs. (21) and (23):

$$\rho \simeq \sum_{ij} \left| \sum_{rs} K_{pq,rs} F_{i-r,j-s} \right| \Big/ \sum_{ij} |K_{pq,ij}|. \tag{24}$$

Since the summations involve all (i, j) and (r, s), and $K_{pq,rs}$ only depends on the differences between indices, $p - r$ and $q - s$, ρ is independent of (p, q). Once ρ is computed, the reduced error estimates for σ_{pq} may be obtained from Eq. (21) after multiplying the first term inside the brackets by ρ.

Our results indicate that the error reduction factor ρ given by Eq. (24) is overly conservative, especially with low-depth resolution interferograms, which require stronger filtering (larger R). More reasonable error estimates are obtained if we assume the applicability of the central limit theorem to the first sum in Eq. (23), over the large number of error terms δu_{ij}. Thus,

$$\rho \simeq \sqrt{\max_{ij} \left(\left| \sum_{rs} K_{pq,rs} F_{i-r,j-s} \right| \right) \times \sum_{ij} \left| \sum_{rs} K_{pq,rs} F_{i-r,j-s} \right|} \Big/ \sum_{ij} |K_{pq,ij}|.$$

Fig. 9 shows surface densities computed from low-pass filtered simulated phase data by combining results from modes 1 to 5 ($\sigma_{1,\ldots,5}$) and modes 1 to 20 ($\sigma_{1,\ldots,20}$). Filters of radii $R = 2, 1, 0.5$ were applied to phase arrays computed from 16, 64 and 256-greylevel ($D = 15, 63, 255$) interferograms, respectively. The results illustrate that filtering results in some loss of information

in the reconstructed density. For system 1 this is observed at internal boundaries between constant density regions, and for system 2 as a loss of contrast in the reconstructions compared with the exact data of Fig. 5d. The loss of detail is greatest for the results obtained from strongly filtered ($R = 2$) low accuracy ($D = 15$) data. Conservative use of filtering can however be employed to speed up data acquisition without significant loss of detail, as in the case of $D = 255$, $R = 0.5$, where the densities recovered from the first 5 modes, compare favourably with those obtained without filtering (Figs. 6 and 7, $\sigma_{1,\ldots,M}$, $M = 5$).

6. Comments on lossy systems

This work assumes that energy losses are sufficiently small, so that resonant responses of the system may be regarded as pure modes of a lossless system. When losses are significant, solution of the inverse problem becomes considerably more complicated. Generalizing Eq. (1), we have

$$F + KU - c\partial_t U = \sigma\partial_t^2 U, \tag{25}$$

where function c is a position-dependent positive damping constant, and F denotes the external applied force per unit area. For harmonic forcing with $F(x, y, t) = f(x, y)e^{-i\omega t}$, and a steady state response $U(x, y, t) = u(x, y)e^{-i\omega t}$, Eq. (25) becomes

$$f + Ku + (ic\omega + \sigma\omega^2)u = 0. \tag{26}$$

Expanding u in terms of natural modes of the corresponding lossless system gives

$$u = \sum_m a_m u_m, \tag{27}$$

where a_m are constants and $u = u_m$ satisfy the free vibration equation (2) for $\omega = \omega_m$. It is convenient to choose normalized modes that satisfy orthogonality relations

$$\int_S u_m K u_n \, dS = -\omega_n^2 \int_S u_m \sigma u_n \, dS = -\delta_{mn}\omega_n^2, \tag{28}$$

where δ_{mn} denotes the Kronecker delta. Substituting Eq. (27) in Eq. (26), pre-multiplying the resulting equation by u_m and integrating over S we obtain

$$a_m = \frac{f_m}{\omega_m^2 - \omega^2 - i\omega\sum_n c_{mn}}, \tag{29}$$

where we have used orthogonality relations (28) and introduced the symbols

$$f_m = \int_S u_m f \, dS, \quad c_{mn} = \int_S u_m c u_n \, dS.$$

When ω is a natural frequency of the lossless system, say $\omega = \omega_l$, and losses are sufficiently small so that

$$\omega \sum_n c_{mn} \ll |\omega_m^2 - \omega^2|, \quad \forall m \neq l, \tag{30}$$

Eq. (29) predicts that the displacement amplitude will essentially be a pure mode, since

$$|a_l| \gg |a_m|, \quad \forall m \neq l,$$

unless $|f_l|$ happens to be small.

In simulating the experimental data presented in Section 5, we have implicitly assumed that relation (30) is satisfied. Density reconstruction for lossy systems, where Eq. (30) is not satisfied, is the subject of a paper currently in preparation.

7. Conclusion

We have demonstrated in principle that a digital imaging interferometer can be used to indirectly measure the mass density of a vibrating membrane. We have analyzed errors arising from finite spatial sampling and signal quantization in the interferograms, and discussed two strategies for reducing such errors, one involving down-sampling and another spatial filtering. Simulation results for inhomogeneous membranes show good agreement with quantitative analysis of the error reduction methods. Results indicate that the surface reconstruction method is practicable when energy losses are small enough to allow observation of pure modes as resonant responses of the system to harmonic excitations. Future work is aimed at extending the method to lossy systems.

References

[1] P.A.A. Laura, R.E. Rossi, R.H. Gutierrez, The fundamental frequency of non-homogeneous rectangular membranes, Journal of Sound and Vibration 204 (1997) 373–376 (doi:10.1006/jsvi.1996.0931).

[2] J.A. Masad, Free vibrations of a non-homogeneous rectangular membrane, Journal of Sound and Vibration 195 (1996) 478–674 (doi:10.1006/jsvi.1996.0454).

[3] C.Y. Wang, Some exact solutions of the vibration of non-homogeneous membranes, Journal of Sound and Vibration 210 (1999) 555–558 (doi:10.1006/jsvi.1997.1270).

[4] C.O. Horgan, A.M. Chan, Vibration of inhomogeneous strings, rods and membranes, Journal of Sound and Vibration 225 (1999) 503–513 (doi:10.1006/jsvi.1999.2185).

[5] R.H. Gutierrez, P.A.A. Laura, D.V. Bambill, V.A. Jederlinic, D.H. Hodges, Axisymmetric vibrations of solid circular and annular membranes with continuously varying density, Journal of Sound and Vibration 212 (1998) 611–622 (doi:10.1006/jsvi.1997.1418).

[6] P.A.A. Laura, D.V. Bambill, R.H. Gutierrez, A note on transverse vibrations of circular, annular, composite membranes, Journal of Sound and Vibration 205 (1997) 692–697 (doi:10.1006/jsvi.1996.0839).

[7] H.P.W. Gottlieb, Exact solutions for vibrations of some annular membranes with inhomogeneous radial densities, Journal of Sound and Vibration 233 (2000) 165–170 (doi:10.1006/jsvi.1999.2806).

[8] D.V. Bambill, R.H. Gutierrez, P.A.A. Laura, V.A. Jederlinic, Vibrations of composite, doubly connected square membranes, Journal of Sound and Vibration 203 (1997) 542–545 (doi:10.1006/jsvi.1996.0818).

[9] I. Elishakoff, Axisymmetric vibration of inhomogeneous clamped circular plates: an unusual closed-form solution, Journal of Sound and Vibration 233 (2000) 727–738 (doi:10.1006/jsvi.1999.2825).

[10] I. Elishakoff, Axisymmetric vibration of inhomogeneous free circular plates: an unusual exact, closed-form solution, Journal of Sound and Vibration 234 (2000) 167–170 (doi:10.1006/jsvi.1999.2826).

[11] S. Homolya, C.F. Osborne, I.D. Svalbe, Effects of signal quantisation and spatial sampling in reconstructing surface density profiles, in: D. Suter, A. Bab-Hadiashar (Eds.), Proceedings of the Sixth "Digital Image

Computing: Techniques and Applications'' Conference, January 21–22, Melbourne, Australia, Australian Pattern Recognition Society, 2002, pp. 297–302.
[12] R. Szilard, Theory and Analysis of Plates: Classical and Numerical Methods, Prentice-Hall, Englewood Cliffs, NJ, 1974.
[13] R. Jones, C. Wykes, Holographic and Speckle Interferometry: A Discussion of the Theory, Practice and Application of the Techniques, Cambridge University Press, Cambridge, 1983.
[14] R.L. Powell, K.A. Stetson, Interferometric vibration analyzis by wavefront reconstruction, Journal of the Optical Society of America 55 (1965) 1593–1598.
[15] P. Hariharan, B.F. Oreb, Stroboscopic holographic interferometry: application of digital techniques, Optics Communications 59 (1986) 83–86.
[16] D.W. Robinson, G.T. Reid, Interferogram Analysis, Digital Fringe Pattern Measurement Techniques, IOP Publishing.
[17] K. Eveker, D. Grow, B. Jost, C.E. Monfort III, K.W. Nelson, C. Stroh, R.C. Witt, The two-dimensional hydrogen atom with a logarithmic potential energy function, American Journal of Physics 58 (1990) 1183–1192.
[18] J.K. Cullum, R.A. Willoughby, Lanczos Algorithms for Large Symmetric Eigenvalue Computations, Birkhauser, Boston, 1985.